Chemistry–A European Journal
Research Article
doi.org/10.1002/chem.202300223
Chemistry Europe
European Chemical Societies Publishing
www.chemeurj.org

Black Titania and Niobia within Ten Minutes – Mechanochemical Reduction of Metal Oxides with Alkali Metal Hydrides

Anna Michaely,[a] Oliver Janka,[a] Elias C. J. Gießelmann,[a] Robert Haberkorn,[a] Haakon T. A. Wiedemann,[b] Christopher W. M. Kay,[b, c] and Guido Kickelbick*[a]

Abstract: Partially or fully reduced transition metal oxides show extraordinary electronic and catalytic properties but are usually prepared by high temperature reduction reactions. This study reports the systematic investigation of the fast mechanochemical reduction of rutile-type TiO_2 and H-Nb_2O_5 to their partially reduced black counterparts applying NaH and LiH as reducing agents. Milling time and oxide to reducing agent ratio show a large influence on the final amount of reduced metal ions in the materials. For both oxides LiH shows a higher reducing potential than NaH. An intercalation of Li^+ into the structure of the oxides was proven by PXRD and subsequent Rietveld refinements as well as ^{6}Li solid-state NMR spectroscopy. The products showed a decreased band gap and the presence of unpaired electrons as observed by EPR spectroscopy, proving the successful reduction of Ti^{4+} and Nb^{5+}. Furthermore, the developed material exhibits a significantly enhanced photocatalytic performance towards the degradation of methylene blue compared to the pristine oxides. The presented method is a general, time efficient and simple method to obtain reduced transition metal oxides.

Introduction

The partial reduction of transition metal oxides (TMO) results in an increase in oxygen vacancies and subsequently in materials with altered electronic properties compared to the original oxides, leading to extraordinary changes in their chemical and physical behavior.[1] A prominent example is the so-called black titania, which was first obtained by Chen et al. via hydrogenation of TiO_2 for 5 days.[2] Due to the introduction of defects and the partial reduction of the Ti^{4+} cations, the material exhibits enhanced photocatalytic activities compared to the pristine oxide. Since then, defect engineering by full or partial reduction of metal ions has become a growing field of research. Today black Nb_2O_{5-x},[3] ZrO_{2-x},[4] WO_{3-x},[5] V_2O_{5-x},[6] and MoO_{3-x}[7] are other prominent examples of this class of materials. Compared to the pristine oxides, the defect-rich counterparts usually exhibit enhanced light absorption[4] as well as improved photocatalytic[6,8] and photoelectrochemical (PEC)[3,9] performance. Besides gas phase hydrogenation,[2,8b] they can also be prepared by annealing at high temperatures in an oxygen-deficient atmosphere,[10] or via chemical reductions, for example, with Mg,[11] Al,[3] or $NaBH_4$.[8a,12] Mechanochemical reduction can lower the required temperatures and therefore the energy consumption in the preparation of such materials. Furthermore, mechanochemical reactions are often faster and additional defects are introduced solely by the impact of the ball milling process, which can also increase the chemical reactivity of the final material. To the best of our knowledge, few mechanochemical approaches for the partial reduction of transition metal oxides have been investigated. Often, the reduction is carried out using highly reactive alkali metals, such as Na[13] or Li[14] or non-conventional hydrides such as TiH_2.[15]

In our study, we used LiH and NaH as readily available alkali metal hydrides and powerful reducing agents in the fast solventless mechanochemical reduction of TiO_2 and Nb_2O_5 at room temperature. While Li^+ (76 pm) has a smaller cationic radius compared to Na^+ (102 pm),[16] NaH exhibits a lower enthalpy of formation and hence a lower stability and thus higher reactivity of NaH ($-56.3\ kJ\,mol^{-1}$) compared to LiH ($-90.5\ kJ\,mol^{-1}$).[17] It can therefore be expected that both hydrides have a different reactivity for the reduction of TMO or reaction behavior such as the involvement of the alkali metal ion during the reaction, which is systematically studied below.

[a] A. Michaely, Dr. O. Janka, E. C. J. Gießelmann, Dr. R. Haberkorn, Prof. Dr. G. Kickelbick
Inorganic Solid-State Chemistry
Saarland University
Campus, Building C4.1, 66123 Saarbrücken (Germany)
E-mail: guido.kickelbick@uni-saarland.de
[b] H. T. A. Wiedemann, Prof. Dr. C. W. M. Kay
Physical Chemistry and Didactics of Chemistry
Saarland University
Campus, Building B2.2, 66123 Saarbrücken (Germany)
[c] Prof. Dr. C. W. M. Kay
University College London
London Centre for Nanotechnology
17–19 Gordon Street, London WC1H 0AH (UK)

Supporting information for this article is available on the WWW under https://doi.org/10.1002/chem.202300223

TiO_2 was chosen for the experiments as it is the most studied oxide for photocatalysis and defect engineering. A lot of studies use anatase-type TiO_2 ($I4_1/amd$) or commercially available P25 due to their high photocatalytic activity. We chose the photocatalytically less active rutile[18] modification ($P4_2/mnm$) for our study because it has a higher mechanical stability than anatase.[19] Similar to TiO_2, H-Nb_2O_5 is also a stable wide-band gap *n*-type semiconductor with $E_g = 3.1$ eV. It is mainly investigated for use in sensors and numerous electronic devices, but there are also some reports on the application of Nb_2O_5 in dye-sensitized solar cells[20] and other photocatalytic applications.[21] Thus, it is worth to further investigate Nb_2O_5 as a potentially promising alternative for TiO_2 for photocatalytic applications. In the following, the influence of the type of reducing agent, milling time and composition on the photocatalytic activity of mechanochemically prepared TiO_2 and Nb_2O_5 is systematically investigated.

Results and Discussion

Crystal chemistry

It is known from the literature that the reduction of oxides with LiH at high temperatures can lead to the incorporation of Li into the oxides, for example, in the reaction of LiH with $BaTiO_3$[22] or Sr_2MnO_4.[23] Therefore, it seems possible that Li is also to some extend inserted into TiO_2 and Nb_2O_5 during the mechanochemical reduction. To facilitate the following discussion about the possible Li intercalation, the crystal chemistry of (lithiated) TiO_2 and Nb_2O_5 will be discussed briefly.

Rutile-type TiO_2 crystallizes in the tetragonal crystal system with space group $P4_2/mnm$ with lattice parameters of $a = 458.0$ pm and $c = 297.0$ pm.[24] In the crystal structure, each Ti^{4+} cation is octahedrally surrounded by oxide anions. These TiO_6 octahedra form chains along [001] via *cis*-edge sharing, the remaining two corners are linked to adjacent strands. Upon insertion of Li, either the tetra- or octahedral sites are occupied (Figure 1a). Using neutron diffraction measurements, Borghols et al. showed that the rutile structure is retained up to a maximum of $Li_{0.07}TiO_2$ ($a = 461.9$ pm, $c = 295.4$ pm).[25] It was shown that the occupation of the tetrahedral sites is energetically favored at low temperatures (10 K), while the occupation of the octahedral sites becomes more favorable at room temperature. For even higher Li contents, for example, $Li_{0.5}Ti_{0.5}O$ the cubic NaCl-type structure ($Fm\bar{3}m$, $a = 414.0$ pm)[26] is observed.[27] Both Li and Ti are octahedrally coordinated by the oxide anions and share the Wyckoff position *4a* (Figure 1b).

For Nb_2O_5 several polymorphs, depending on the synthesis temperature, have been reported. The monoclinic high temperature phase H-Nb_2O_5 crystallizes with space group $P2/m$ and lattice parameters of $a = 1933.0$ pm, $b = 382.3$ pm, $c = 2032.2$ pm and $\beta = 115.8°$.[28] The Wadsley-Roth phase consists of blocks formed by 3×5 and 3×4 [NbO_6] octahedra. These are connected by common corners within a block; however, edge sharing is observed between these entities. Finally, the tetrahedrally coordinated niobium site in H-Nb_2O_5 is only half-occupied.[29] Different lithiated Nb-oxides have been described for example, by Cava et al.[28] who identified five cavities in H-Nb_2O_5. Catti and Ghaani[30] characterized lithiated H-Nb_2O_5 ($Li_{1.714}Nb_2O_5$) via neutron diffraction experiments and localized the Li^+ cations in four-fold nonplanar, distorted tetrahedral and distorted square-pyramidal voids (Figure 1c), in line with the positions proposed by Cava et al. However, the localization of the Li atoms leads to a reduction in symmetry ($P2$, $a = 1913.2$ pm, $b = 413.5$, $c = 2014.2$ pm, $\beta = 119.57°$).[30]

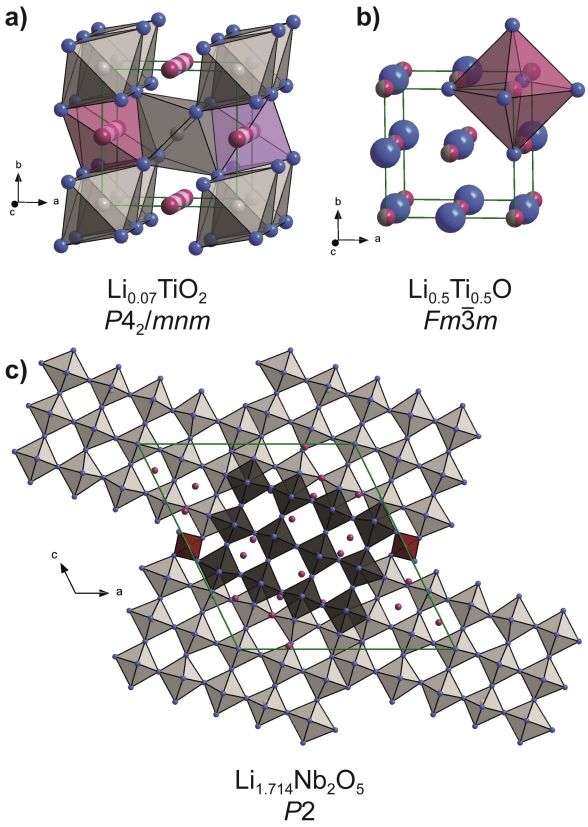

Figure 1. (a) Crystal structure of lithiated rutile-type $Li_{0.07}TiO_2$,[25] tetrahedrally coordinated Li atoms are shown in purple, octahedrally coordinated Li atoms are pink, Ti atoms are shown in gray and oxygen atoms in blue. (b) Crystal structure of NaCl-type $Li_{0.5}Ti_{0.5}O$,[26] Li atoms are purple, Ti atoms are shown in gray and oxygen atoms in blue. (c) Crystal structure of lithiated H-Nb_2O_5.[30] The 3×4 block of octahedrally coordinated Nb atoms in H-Nb_2O_5 is shown in dark gray, the 3×5 block in light gray, the tetrahedrally coordinated Nb atoms are drawn in red. The space groups are given.

Optical color change after ball milling

The partial reduction of TiO_2 and Nb_2O_5 by a mechanochemical route was performed by milling the TMO with *n* equivalents of LiH and NaH ($n = 0.5$, 1 and 2) for 10, 30, and 60 min at a fixed milling speed of 300 rpm. In the following, the samples are denoted as *NM_n:m_t*. The first letter being T for TiO_2 or N for Nb_2O_5, the second letter corresponds to the alkali metal hydride (N = NaH, L = LiH), while *n* and *m* represent the number of

equivalents of TiO_2/Nb_2O_5 and the hydride, respectively. Finally, *t* represents the milling time in minutes.

After only 10 minutes of ball milling at room temperature, a visually perceptible color change of the powders from white to light gray in the case of TiO_2 or brownish-gray to dark blue-black for Nb_2O_5 was observed. The obtained coloration is clearly depending on the amount of hydride added (Figure 2). The observed coloration of the samples after ball milling is most likely caused by the reduction of Ti^{4+} to Ti^{3+}[31] and of Nb^{5+} to Nb^{4+}.[32] However, for reasons of electroneutrality, the reduction must be either accompanied by the intercalation of alkali metal ions or the formation of oxygen vacancies, which also can give rise to color centers.[10b] Also a combination of both effects seems possible. Therefore, ball milling of the oxides in the presence of the reducing agents should produce various types of defects in the compounds. For both oxides, the milled powders have a darker color when LiH was used as the reducing agent compared to samples reduced under the same conditions applying NaH. Usually, NaH would be expected to have a higher reductive power and therefore we expected the darker color in the corresponding samples. This assumption is based on the size difference of the alkali metal ions (Li^+: 76 pm, Na^+: 102 pm)[16] and on the lower enthalpy of formation and thus also the lower stability and thus higher reactivity of NaH ($-56.3\ kJ\,mol^{-1}$) compared to LiH ($-90.5\ kJ\,mol^{-1}$).[17] It has already been reported that Li-containing reducing agents can behave differently due to the incorporation of Li into the oxide,[22] which could also be the reason for the apparent higher reactivity of LiH in our study.

With the EASY GTM system for the Fritsch Pulverisette 7 *premium line*, we can monitor the development of temperature and pressure in the grinding bowl. A continuous increase in pressure up to several bar can be observed, which is due to the development of hydrogen with increasing milling time. At the same time, the temperature also increases, but remains below 35 °C (Figure S1, Supporting Information).

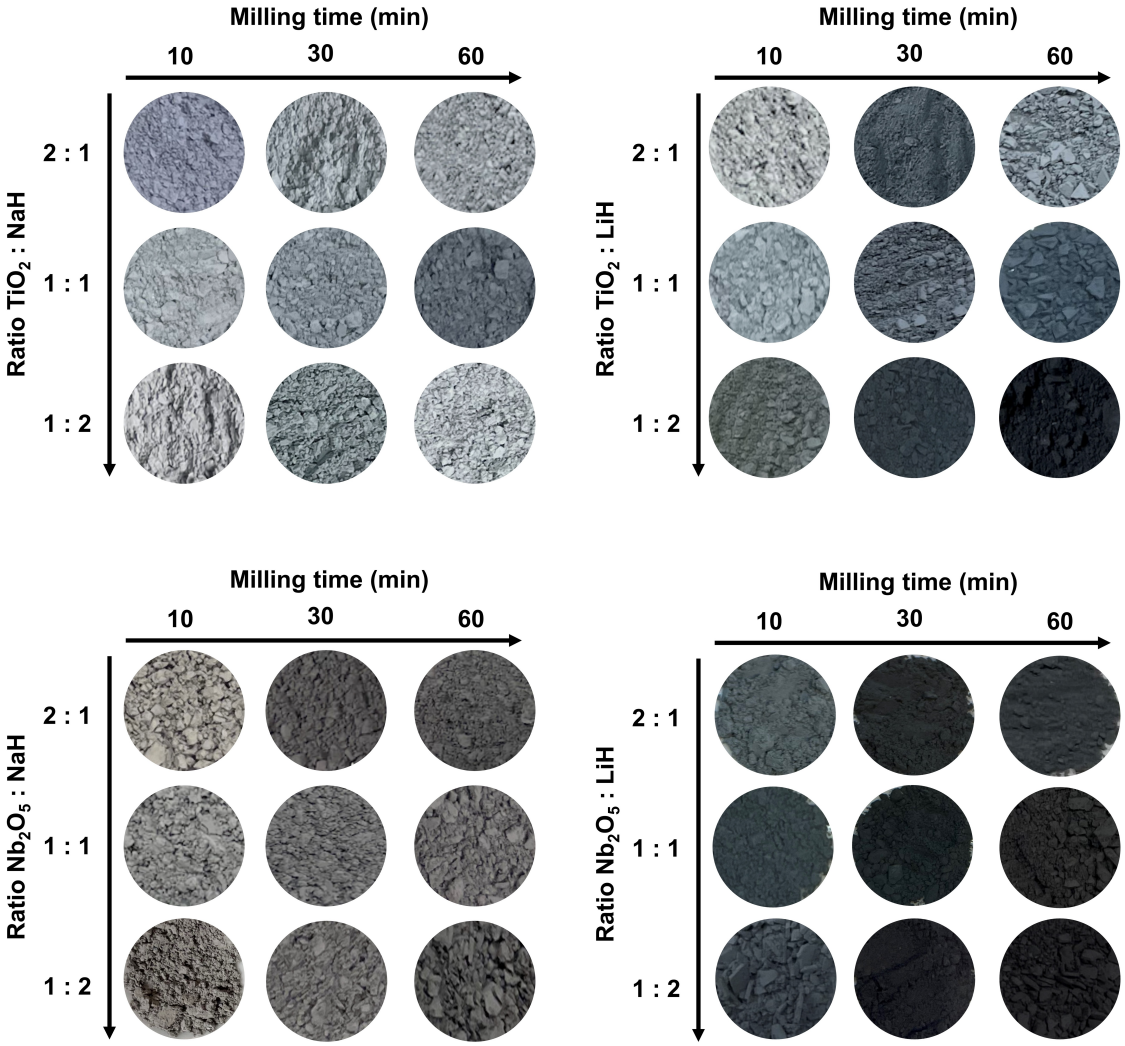

Figure 2. Photographs of reduced TiO_2 and Nb_2O_5 obtained after milling with NaH and LiH at various molar ratios between 10 and 60 min at a constant milling speed of 300 rpm.

Powder X-ray diffraction analysis

Powder X-ray diffraction (PXRD) patterns were recorded to gain a better understanding of the processes during ball milling and to analyze possible changes in the crystal structure due to the partial reduction. No significant changes in the PXRD patterns are observed after milling TiO_2 (rutile, $P4_2/mnm$) with NaH (NaCl-type, $Fm\bar{3}m$). The observed powder pattern still corresponds to rutile-type TiO_2. Contrary, the reflections at around 27.4° (110) and 54.0° 2θ (211) show a strong asymmetry after ball milling with LiH (NaCl-type, $Fm\bar{3}m$) caused by an increasing amount of disorder due to the reaction with LiH (Figure 3a). Both reflections are dominated by changes of the *a* lattice parameter of TiO_2, indicating that the structural changes such as the intercalation of Li^+[33] and the formation of oxygen vacancies mainly influence the *ab*-plane.[34] To accommodate for these structural changes in the Rietveld refinement, a multi-fraction model with different fractions of rutile-type TiO_2 was used (Figure S2-6, Supporting Information). Moreover, the reflections at ~44° (200) and ~63° 2θ (220) are significantly broadened due to an overlap with newly emerging reflections corresponding to the cubic $Li_{0.5}Ti_{0.5}O$ phase with a rock salt-type structure ($Fm\bar{3}m$) (Figure S6, Supporting Information) exhibiting titanium in the oxidation state +III. This observation is in line with the formation of $Li_{0.5}Ti_{0.5}O$ when rutile-type TiO_2 is lithiated via more conventional reagents such as *n*-BuLi[33b] or hydrothermally with LiOH,[35] but can also be achieved by grinding the oxide with Li.[33b]

The fraction of $Li_{0.5}Ti_{0.5}O$ increases with longer milling time and higher amounts of initial LiH (Figure 3b), for example from 9 to 44 wt% after milling with 2 equiv. LiH for 10 and 60 min, respectively. The increase of the Li-containing phase with increasing milling time was proven by the determination of the Li to Ti ratio by ICP-MS measurements. After milling TiO_2 for 10 and 60 min with 2 equiv. LiH, a molar Li:Ti ratio of 0.08:1 and 0.38:1 was determined. These results are in good agreement with the results of the Rietveld refinements, which gave an overall composition of $Li_{0.09(1)}TiO_2$ and $Li_{0.36(1)}TiO_2$ for the samples TL_1:2_10 and TL_1:2_60, respectively. The presence of Li inside the sample is further proven by ^{6}Li solid-state NMR (see below) In contrast, no sodiation was observed in TiO_2 reduced with NaH after reduction, possibly due to the larger radius of Na^+ compared to Li^+. A similar change in color and lithiation was also observed after ball milling anatase-type TiO_2 ($I4_1/amd$) with LiH. In addition to the transformation of anatase into the orthorhombic high-pressure form (α-PbO_2-type, *Pbcn*), which is known to occur during milling,[36] orthorhombic $Li_{0.5}TiO_2$ (*Imma*) was also formed (Figure S12, Supporting Information).

For Nb_2O_5, no significant changes in the crystal structure are observed by PXRD measurements after milling with both hydrides. The observed diffraction patterns still correspond to monoclinic H-Nb_2O_5 ($P2/m$) regardless of the reducing agent and milling time (Figure S13a, Supporting Information). However, the unit cell volumes revealed an increase for Nb_2O_5 upon reduction with LiH, whereas no significant increase was observed for NaH (Figure S13b, Supporting Information). Only lithiated, but no sodiated Nb_2O_5 phases have been reported in the literature, where the crystal structure was maintained during the intercalation of the alkali metal ions,[30] which is again due to a smaller ionic radius of Li^+ compared to Na^+.[16] Hence, the increase of the unit cell volume of several Å^3 can be attributed to an intercalation of Li^+,[28,30] whose presence is also proven by ^{6}Li solid-state NMR (see below). Based on the increase of the unit cell volume of LiH reduced samples, a sample composition between $Li_{0.02(1)}Nb_2O_5$ and $Li_{0.25(1)}Nb_2O_5$ was calculated (Table S2, Supporting Information).

Elemental analysis (CHN) of sample TL_1:2_60 revealed that no significant amount of hydrogen is found, indicating that no hydrogen is introduced into the crystal structure. Therefore, no Ti–OH or Ti–H bonds are formed, as it is sometimes reported for black titania prepared by hydrogenation.[2,37] However, the formation of these bonds strongly depends on the synthesis conditions[1] and open questions about the actual structure remain.[38] Since no significant hydrogen concentration was detectable, the hydride ion will most likely transfer one or two electrons to the oxide[39] during the ball milling process, followed by the reduction of Ti^{4+}/Nb^{5+} to Ti^{3+}/Nb^{4+} along with the formation of oxygen vacancies or the insertion of Li^+ to respect charge neutrality. It is also possible that the mechanochemical reduction process follows an even more complicated

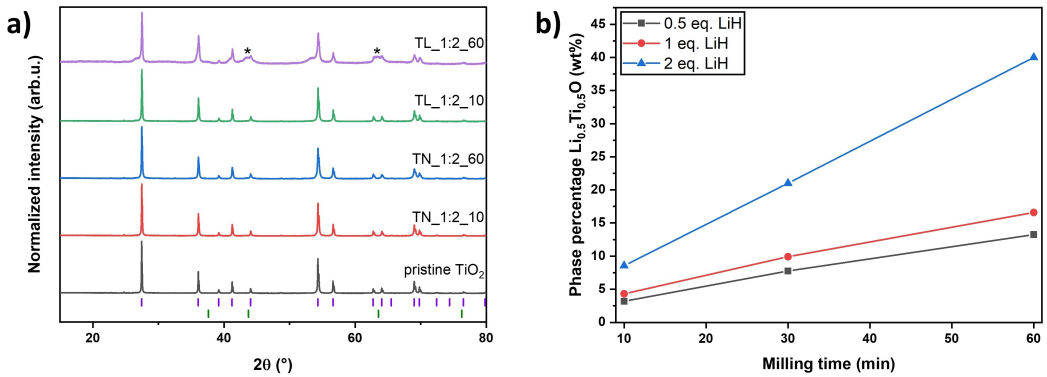

Figure 3. (a) PXRD patterns of pristine and reduced titania. Violet ticks indicate the Bragg positions of rutile-type TiO_2 ($P4_2/mnm$) and green ones of $Li_{0.5}Ti_{0.5}O$ ($Fm\bar{3}m$). The position of the most intense reflections of the latter are marked with asterisks. (b) Phase percentage of $Li_{0.5}Ti_{0.5}O$ versus milling time and LiH amount, obtained by Rietveld refinement.

reaction mechanism,[23] but no experimentally proven mechanistic details can be given currently.

TGA measurements

In a next step, TGA measurements were performed to investigate the re-oxidizability of the samples by heating them under nitrogen to 600 °C followed by heating under synthetic air to 900 °C to see if a reoxidation, which is accompanied by a mass increase, takes place.[40] After the thermal treatment, all samples turned white again due to the reoxidation of Ti^{3+}/Nb^{4+} to Ti^{4+}/Nb^{5+} during the formation of alkali metal titanates or niobates and/or the refilling of oxygen vacancies.[7,41] In most samples, no significant mass gain was observed, most likely due to the low degree of reduction. Only for TL_1:2_60 and NL_1:2_60 a mass gain of 1.4 and 0.7% due to the uptake of oxygen was observed, respectively (Figure S14, Supporting Information). PXRD measurements confirmed that in all samples the reoxidation of Ti^{3+} and Nb^{4+} to Ti^{4+} and Nb^{5+} occurred. While samples with a lower degree of reduction or samples reduced via NaH were simply reoxidized to TiO_2 and Nb_2O_5, lithium titanates and niobates such as $Li_4Ti_5O_{12}$ ($Fm\bar{3}m$)[42] and $LiNb_3O_8$ ($P2_1/c$)[43] were formed from higher reduced samples (Figure S15, Supporting Information). The color change of TiO_2 if heated under air in absence of a sodiation reaction (Figure S16, Supporting Information) leads to the conclusion, that oxygen defects according to TiO_{2-x} can form in principle. However, since the formation of the before mentioned Li-titanates and Li-niobates can also only occur upon oxygen uptake, a differentiation between reduction via lithium intercalation and reduction due to oxygen vacancies is not possible.

^{6}Li solid-state NMR experiments

Solid-state MAS NMR investigations of ^{6}Li or ^{7}Li nuclei are a powerful technique to probe the local environment of the Li^+ ions in their respective host structures as for example shown for TiO_2.[44] And although the differences in the chemical shifts are small ($\delta = -1$ to 1 ppm), a site assignment was possible. Figure 4a shows a comparison of the ^{6}Li MAS NMR spectra of the LiH reduced TiO_2 samples after 10, 30 and 60 minutes of milling. The presence of a resonance near $\delta \sim 1$ ppm clearly proves the presence of Li in the solid. The increasing intensity of the NMR signal is proportional to the milling times suggesting that more Li is present in the samples since the measurement conditions for the NMR spectra (number of scans, acquisition time, pulse sequence, delay time) were kept the same for all samples. In addition, the full width at half maximum (FWHM) of the signal increases with prolonged milling times (Table S5, Supporting Information), indicating higher structural disorder. A deeper analysis of the individual spectra using the DMFit software program package showed that the line shape varies significantly. Gaussian-Lorentz fit functions were used for analysis of the asymmetry of the peaks (Figure 4b, d, f and Table S5, Supporting Information). All samples show a broad asymmetric signal over the range from −5 up to 9 ppm. The maximum of the resonance can be observed around $\delta \sim 1$ ppm, which is typical for ionic, diamagnetic Li species.[45] For the reduced samples with a milling time of 10 minutes, the line shape can be described well with a single line fit. In contrast, single line fits applied to the spectra obtained from the longer milled samples (30 and 60 min) show a rather bad agreement with the experimental data. The intensity profile, at higher and lower frequencies, cannot be described in a satisfactory way. Especially the intensity in the region between 5 to 8 ppm seems to be caused by a signal originating at least one other Li species. The addition of a second signal (Gaussian-Lorentz function) indicated that this resonance is centered around $\delta =$ 8.4 ppm, however, an extremely large FWHM is found (Figure 4c, e).

When comparing this data to the literature[44a–d] it becomes clear that the presented spectra are rather broad and featureless. Even in ball-milled samples of Li-titanates, synthesized by a high temperature solid-state approach, structural information about the location of the Li ions within the structures could be obtained due to sharp lines and the sensitivity of ^{6}Li to the structural and electronic environment.[44e] This is in total contrast to the measurements performed here because no detailed insight about the coordination of Li^+ in the structure could be obtained. Therefore, it can be concluded that these systems exhibit significant disorder resulting in many different crystallographic Li sites, which leads to a large variation of the Li–O bond lengths and in turn to the observed line broadening. The broad resonance with its large shift of $\delta \sim 8$ ppm, though disagrees with the previously mentioned NMR studies. However, NMR investigations on paramagnetic $LiCoO_2$ reported resonance shifts of up to 17 ppm.[45] The intermetallic compound Li_4Pt_3Si shows even resonance shifts of up to ~120 ppm.[46] Here the nuclear magnetic moment interacts with the magnetic moment of the Co atoms in the case of $LiCoO_2$ or the conduction electrons of Li_4Pt_3Si leading to these drastic shifts known as Knight shifts. Since the reduced TiO_2 shows a black color, but is not metallic in nature, the signal at $\delta \sim 8$ ppm could be explained from the interactions of the paramagnetic Ti^{3+} centers with the Li nuclei similar to $LiCoO_2$.[45] This hypothesis is further strengthened by the fact that the signal at $\delta \sim 8$ ppm increases in intensity with prolonged ball milling time and the recorded electron paramagnetic resonance (EPR) spectra (see below). Finally, the ^{6}Li NMR spectrum of LiH reduced Nb_2O_5 (1:2 ratio) after 60 min ball milling was exemplarily also fitted with a single Gaussian-Lorentz line (Figure S17, Supporting Information). The main resonance shows a chemical shift around $\delta \sim 1$ ppm with a comparable FWHM (Table S5, Supporting Information).

Electron paramagnetic resonance spectroscopy

EPR spectroscopy was used to detect and further investigate the presence of unpaired electrons at the Ti^{3+} and Nb^{4+} centers. According to Chester et al., the hyperfine structure of their niobium-doped rutile only showed hyperfine splitting at

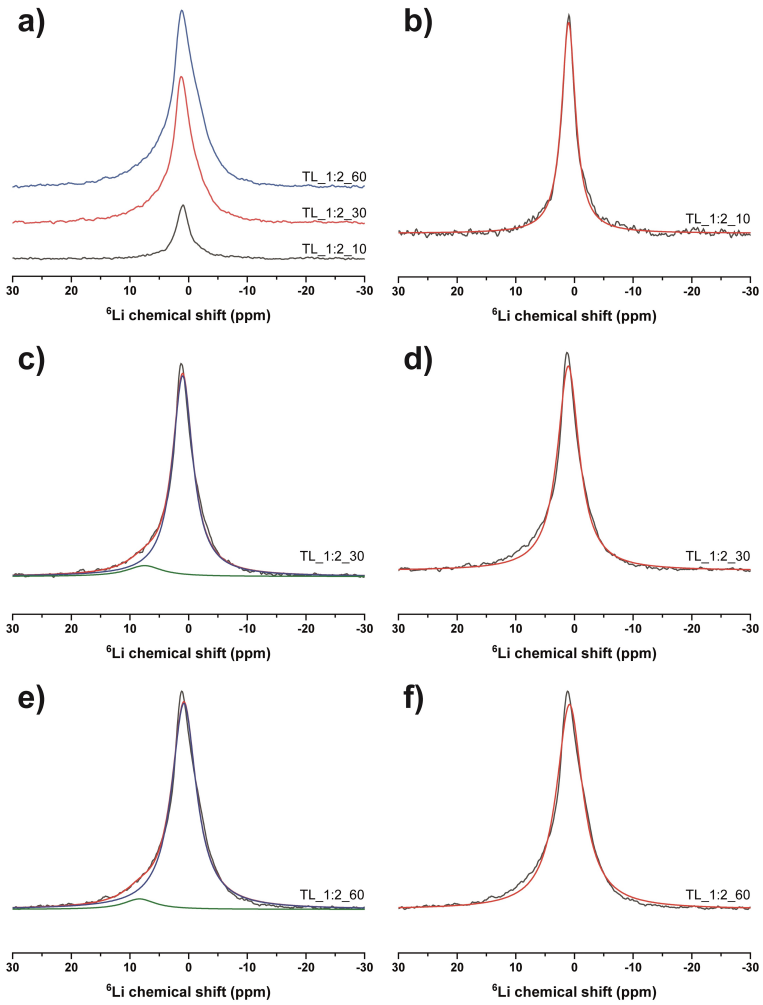

Figure 4. (a) ^{6}Li MAS NMR spectra of TiO_2 + LiH (1 : 2) after ball-milling of 10 (gray), 30 (red) and 60 (blue) minutes. (b, d, f) Individual ^{6}Li MAS spectra for the given ball milling times fitted with a single Gaussian-Lorentz line. ^{6}Li MAS spectra for TiO_2 + LiH after a milling time of (c) 30 and (e) 60 minutes fitted with two lines. Spectra are plotted in black; red lines are the fitting curves; the blue and green lines indicate the individual spectral components.

temperatures below 25 K.[47] Therefore, the EPR experiments were conducted at 10 K. EPR experiments above 10 K showed a broad signal without hyperfine lines, which was a first qualitative evidence for the presence of unpaired electrons in both reduced titania and niobia samples. The observed EPR signal (Figure 5) could be caused by paramagnetic oxygen vacancies V_0, as well as Ti^{3+} and other lower valence Ti species, as documented for many oxide materials.[48] The formation of

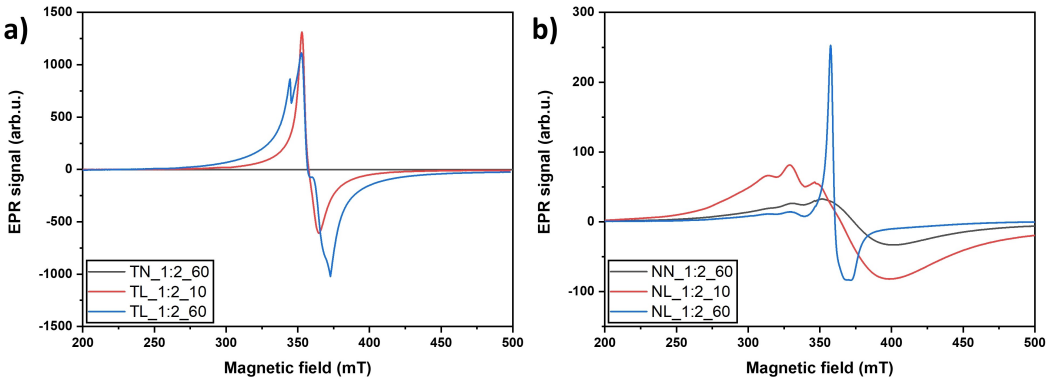

Figure 5. Continuous wave (CW) EPR spectra of NaH (black line) and LiH (blue and red lines) reduced (a) TiO_2 and (b) Nb_2O_5 samples.

unpaired electrons during the mechanochemical reduction of TiO_2 with LiH could be confirmed, while the NaH reduced TiO_2 only showed a weak intensity signal. To differentiate and compare the different ball milling times, the peak areas of the reduced oxides were compared. As expected, for samples obtained after prolonged milling, the peak area increases with milling time.[14] Thus, the longer the milling time, the more Ti^{4+} ions are reduced to Ti^{3+}, which is accompanied by the formation of oxygen vacancies or the intercalation of Li.

The formation of unpaired electrons during the mechanochemical reduction of Nb_2O_5 with LiH/NaH could be confirmed as well, but with lower intensities and peak areas and thus, fewer paramagnetic species. The Nb^{4+} concentration shows the same time dependency as in titania with a higher formation of oxygen vacancies and Li intercalation with prolonged milling duration. Theoretically, a total of ten instead of the three visible lines would be expected for $^{93}Nb^{4+}$ due to hyperfine coupling since niobium has a nuclear spin of 9/2 (100% natural abundance). Similarly, a total of six lines is expected for $^{47}Ti^{3+}$ ($I=5/2$, 7.4% natural abundance) and eight lines for $^{49}Ti^{3+}$ ($I=7/2$, 5.4% natural abundance) but ~87% of the Ti centers have no spin, and therefore no coupling. The total number of lines does not match the expectation, but hyperfine splitting constants could be derived from the visible peaks. For the TiO_2/LiH system, 7.9 mT and for the Nb_2O_5/LiH system, 17.8 mT, were extracted.

Raman spectroscopy

In order to further investigate the structural changes, Raman spectra were recorded. Both pristine and reduced titania show the typical Raman signals of rutile at 143, 240, 446 and 609 cm^{-1}, which can be assigned to the Raman modes B_{1g}, second-order scattering, E_g and A_{1g} (Figure 6a).[49] Similarly, the typical Raman bands of monoclinic H-Nb_2O_5, namely Nb–O–Nb angle-deformations between 160 to 300 cm^{-1}, transverse optic modes (TO) originating from symmetric stretching of NbO_6 octahedra between 600 and 700 cm^{-1} and the longitudinal optic mode (LO) of NbO_6 edge-shared octahedra at around 990 cm^{-1} were observed for all Nb_2O_5 samples (Figure 6b).[50] No major changes are observed for NaH reduced oxides in both cases, suggesting that only minor structural changes, for example introduction of oxygen defects, occurred during the mechanochemical reduction. In case of LiH reduced TiO_2 a redshift of up to 10 cm^{-1} of the multi-photon band at around 230 cm^{-1} and a blueshift of 15 cm^{-1} of E_g is observed, while a red shift of up to 8 cm^{-1} occurred of the LO mode of the symmetric Nb–O stretching of LiH reduced Nb_2O_5. Furthermore, the Raman bands become more broadened the more reduced the samples are due to the increase of structural disorder for example, due to Li intercalation[51] or formation of other defects during the ball milling process.[52]

Compared to the pristine oxides, all reduced samples exhibit a significantly stronger absorption in the visible region

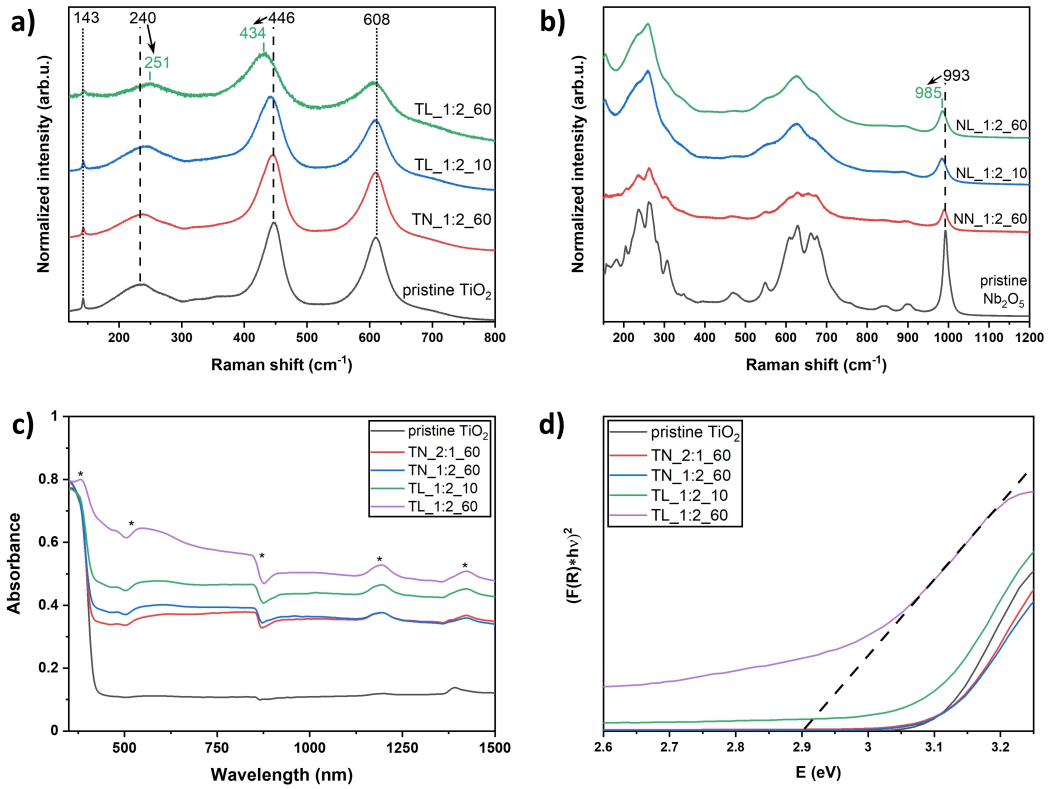

Figure 6. Raman spectra of pristine (black) and with 2 equiv. NaH (60 min, red) and LiH (10 min, blue; 60 min, green) reduced (a) TiO_2 and (b) Nb_2O_5, (c) DRS-UV-Vis absorbance spectra and (d) Kubelka-Munk plot of pristine and reduced TiO_2. Lamp, detector, and filter changes in c) are marked with an asterisk, the evaluation of the band gap is shown by the dashed line in d).

(Figure 6c) as shown via the UV-Vis diffuse reflectance spectra (DRS). A clear correlation between the color of the samples and the absorbance of visible light was observed. The values of the optical band gaps and their changes during the reduction were obtained based on the Kubelka-Munk function $F(R)$ and the Tauc relationship $(F(R)h\upsilon)^{\frac{1}{n}} = A(h\upsilon - E_g)$ with $h\nu$ being the photon energy, A is a proportionality constant, E_g the band gap energy and n a parameter depending on the type of band gap. For direct allowed electronic transitions n equals $\frac{1}{2}$ and for indirect allowed transitions n equals 2.[53] According to literature, rutile-type TiO_2 and monoclinic H-Nb_2O_5 both have a direct band gap.[54] In both cases, the optical band gap of the reduced oxides is significantly lowered (up to 0.4 eV compared to the pristine oxide) due to the partial reduction and introduction of defects (Figure 6d, Figure S18, Table S6, Supporting Information)).[14]

Photocatalytic degradation experiments

Often, a reduction in the band gap and absorption properties over a wider range of wavelengths leads to improved (photogenerated) charge carrier properties and higher photocatalytic activity.[14] To evaluate the photocatalytic activities of the reduced oxides compared to the pure oxides, the photochemical degradation of methylene blue (MB), commonly used in tests of the photocatalytic activity of heterogeneous catalysts and found as a pollutant in the wastewater of the textile industry, was studied.[55] For the experiments under UV irradiation, a light source emitting 365 nm was used, while the wavelengths emitted by the visible light source range from 400 to 700 nm with the strongest irradiance being at around 450 and 550 nm. Blank experiments show that without the addition of a catalyst, the photobleaching of MB is only minimal (Figure 7). Overall, no enhancement is observed for NaH reduced TiO_2 and Nb_2O_5 samples, possibly due to the small degree of reduction. In contrast, all LiH reduced samples exhibit an improved performance compared to the pristine oxides. When visible light was used for the degradation experiments, about 33% of the MB was degraded after 5 h using untreated rutile-type TiO_2 was used as catalyst. When a LiH reduced TiO_2 sample was used milled for 10 and 60 min, a significant increase to 45 and 70% of the degraded MB was observed in the same period (Figure 7a). Due to the successful introduction of defects and the partial reduction of Ti^{4+} to Ti^{3+}, the synthesized materials even show a higher photocatalytic activity under visible light compared to the commercially available and widely used photocatalyst Evonik P25 (Figure 7a), which consists of both anatase and rutile TiO_2. In the case of H-Nb_2O_5 only a slight enhancement of the photocatalytic performance of the LiH reduced sample obtained after 10 min of milling ($C_t/C_0 = 0.69$) was observed compared to pristine H-Nb_2O_5 ($C_t/C_0 = 0.72$). LiH treated Nb_2O_5 obtained after 60 min of ball milling in contrast shows a significant improvement since a MB conversion of 65%

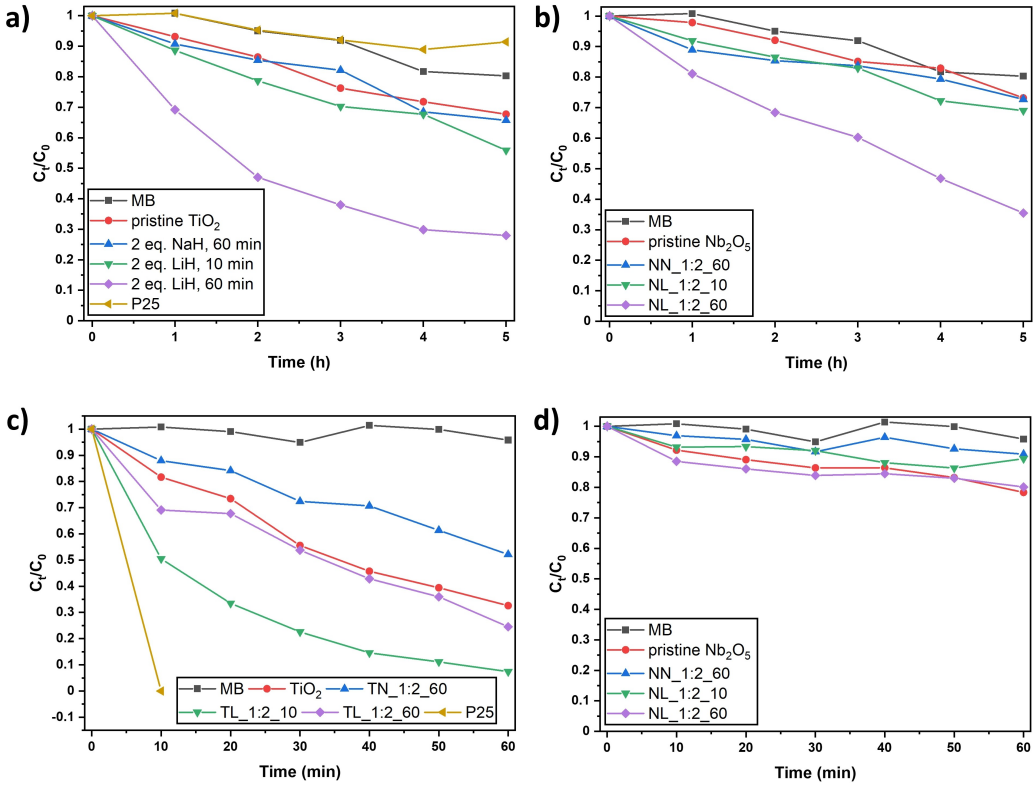

Figure 7. Photocatalytic degradation of methylene blue (MB) (a), (b) under visible light and (c), (d) under UV (365 nm) light without catalyst (black), with pristine titania and niobia (red) and with reduced titania and niobia (blue: NaH, 60 min; green: LiH, 10 min; purple: LiH, 60 min) and with commercially available P25 (yellow). Note the different time scales between (a, b) and (c, d).

was achieved after 5 h of irradiation (Figure 7b). It can therefore be concluded that longer milling times and thus a higher degree of reduction for the LiH reduced samples favor the degradation of MB using visible light. In contrast, under irradiation with UV light (365 nm) a complete discoloration of the MB solution was achieved after only 60 min using the LiH reduced titania sample obtained after 10 min of milling ($C_t/C_0 =$ 0.07). Interestingly, both pristine rutile TiO_2 and the LiH reduced sample (60 min) exhibit a lower photocatalytic activity in the UV range (Figure 7c). In comparison to the standard photocatalyst P25, our prepared materials show a somewhat lower photocatalytic activity since a complete discoloration of the MB solution can be achieved with these tailor-made materials after only 10 min with P25 under UV irradiation (Figure 7b). This is attributed to the fact that our sample still predominately composed of photocatalytically less active rutile. As for the niobia samples, both pristine and reduced niobia show almost no activity in the UV range (Figure 7d), which makes the reduced titania samples the more suitable for photocatalytic applications, especially in the UV range.

To exclude that the enhancement of the photocatalytic properties only originates from ball milling, TiO_2 was milled for 60 min and its photocatalytic activity was measured under both UV and visible light. In general, mechanochemistry is a suitable method for the preparation of catalysts.[56] While some publications report an enhancement of the photocatalytic activity of oxides,[57] sulfides[58] or composite materials[59] depending on the milling conditions, no enhancement was observed compared to pristine rutile-type TiO_2 in the present case (Figure S19, Supporting Information), in contrast to the already active anatase phase cited above. This shows that the mechanochemical reaction with the alkali metal hydrides is the main reason for the faster MB degradation. The higher activity of the synthesized materials can be ascribed to the presence of defects such as Ti^{3+}/Nb^{4+}, resulting in a smaller band gap and consequently a better absorption of light, as well as a probable reduction of the recombination rate of photogenerated electron-hole pairs.[11a,14]

In literature, there are some reports on the use of rock salt-type $Li_{0.5}Ti_{0.5}O$ as a catalyst for the photocatalytic dye degradation[35a] and hydrogen generation.[60] Since the compounds formed during ball milling of TiO_2 and LiH, $Li_{0.5}Ti_{0.5}O$ was prepared via a solid-state reaction under argon using TiO_2 and 2 equiv. LiH (Figure S20, Supporting Information). The reaction mixture was heated to 600 °C for 60 min. Afterwards, the obtained material was washed with NH_4Cl/MeOH and MeOH. As a proof of concept that not all measured effects of reduced titania samples are caused by $Li_{0.5}Ti_{0.5}O$, its photocatalytic activity was compared with the photocatalytic activity of TL_1:2_60 under visible light irradiation and with TL_1:2_10 under UV (365 nm) irradiation. As shown in Figure 8, $Li_{0.5}Ti_{0.5}O$ performs slightly better under visible irradiation than TL_1:2_60 but shows a poor performance under UV irradiation. This suggests that not all observed effects originate from the presence of $Li_{0.5}Ti_{0.5}O$ such as the good MB degradation ability under UV light of our synthesized material, but it seems that $Li_{0.5}Ti_{0.5}O$ might be especially beneficial for an effective MB degradation under visible light irradiation.

Conclusion

In summary, a simple and rapid room temperature mechanochemical process was developed for the reduction of rutile-type TiO_2 and H-Nb_2O_5 using alkali metal hydrides. Depending on the synthesis conditions (type and amount of reducing agent and milling duration), samples with a color ranging from light gray to blue to gray and black were obtained. In general, longer milling times and higher amounts of the reducing agent resulted in a higher degree of reduction of the transition metal ions. After reduction using NaH, no significant changes in the crystal structure were observed from PXRD measurements, but the formation of cubic $Li_{0.5}Ti_{0.5}O$ and the intercalation of Li was observed for TiO_2 and Nb_2O_5 when reduced with LiH. The intercalation may occur due to the smaller radius of Li^+ compared to Na^+. The band gap of the ball milled transition metal oxides decreased by up to 0.4 eV, while more paramagnetic centers were formed with longer milling time, as shown by EPR spectroscopy. ^{6}Li NMR spectroscopic investigations clearly demonstrate that the samples contain significant

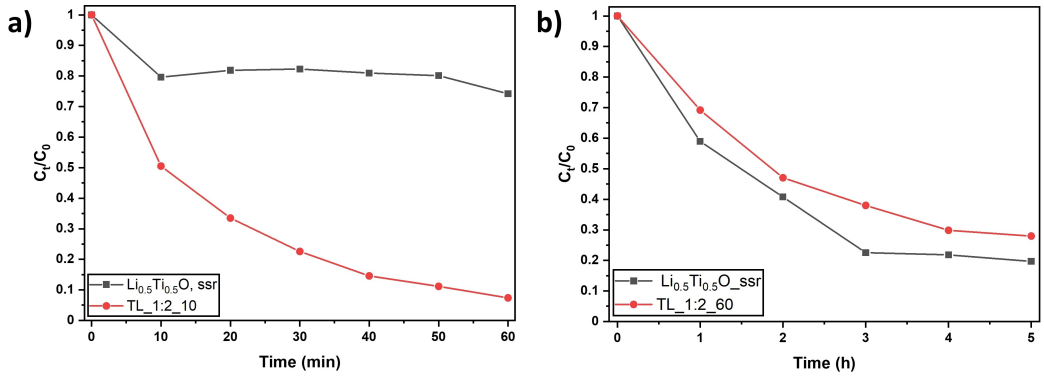

Figure 8. Photocatalytic degradation of MB with $Li_{0.5}Ti_{0.5}O$ prepared by solid state reaction and LiH reduced titania (60 min and 10 min) under (a) visible and (b) UV (365 nm) light.

amounts of disorder since the signals are featureless. In the case of LiH reduced TiO_2 milled for 30 or 60 min, a second signal arises that could be attributed to the interaction of the paramagnetic Ti^{3+} ions with the Li nucleus. Raman spectroscopy revealed an increase in structural disorder due to the formation of defects. These are more pronounced when LiH is used, as indicated by the darker color of the reduced oxides. Due to these defects, a significantly better photocatalytic performance of the synthesized materials compared to the pristine oxides was achieved under illumination with both UV and visible light.

Experimental Section

Materials: Nb_2O_5 (ChemPur, Karlsruhe, Germany, 99.98%), TiO_2 (Alfa Aesar GmBH, Karlsruhe, Germany, 99.5%), LiH (Alfa Aesar GmBH, Karlsruhe, Germany, 99.4%), and NaH (Merck, Darmstadt, Germany, >98%) were used without further purification and stored in a glovebox under argon atmosphere. All solids have been characterized by powder X-ray diffraction before use.

Synthetic procedures: The syntheses were performed in a planetary ball mill Pulverisette 7 *premium line* (Fritsch, Idar-Oberstein, Germany) using ZrO_2 grinding jars with a volume of 45 mL and 180 Y-stabilized ZrO_2 milling balls with a diameter of 5 mm. All syntheses were performed under inert gas by filling and closing the milling jars in an argon filled glovebox. For the ball milling experiments 3.00 g of Nb_2O_5 (11.29 mmol, 1 equiv.) or TiO_2 (37.6 mmol, 1 equiv.) were milled with *n* equiv. of LiH or NaH ($n = 0.5$, 1 and 2). The milling speed was set to 300 rpm, and the milling time was varied from 10 to 30 to 60 min.

Afterwards, the samples were washed with 0.1 M NH_4Cl/MeOH and MeOH under argon several times to remove unreacted alkali metal hydrides as well as side products. Both solvents were degassed with argon for 1 h beforehand. After centrifugation, samples were dried in a vacuum oven at 80 °C and stored in an argon-filled glovebox.

Testing of the photocatalytic activity: The photocatalytic experiments were performed in an EvoluChem™ PhotoRedOx Box (HepatoChem, Beverly, USA) equipped with 2×20 ml sample holder, an EvoluChem 365PF lamp (365 nm) for testing the photocatalytic activity in the UV region and an Evoluchem 6200PF lamp (cold white) for the Vis region.

In a typical methylene blue (MB) degradation experiment, 15 mg of catalyst (1 mg/ml) were added to 15 mL of an aqueous MB solution (20 ppm). After stirring for 30 min in the dark, the suspensions were irradiated. After certain time intervals, 0.4 ml of suspension were periodically sampled and centrifuged to separate the photocatalyst from the solution. The MB solution was then diluted by a factor of 2 before the concentration of MB was measured by UV-Vis spectroscopy (PerkinElmer Inc., Shelton, USA).

Characterization: Powder X-ray diffraction (PXRD) patterns were recorded on a D8-A25-Advance diffractometer (Bruker AXS, Karlsruhe, Germany) under ambient conditions in Bragg-Brentano θ-θ-geometry (goniometer radius 280 mm) with Cu K_α-radiation ($\lambda = 154.0596$ pm). A 12 μm Ni foil served as a K_β filter at the primary beam side. At the primary beam side, a variable divergence slit was mounted and a LYNXEYE detector with 192 channels at the secondary beam side. Experiments were carried out in a 2θ range of 7 to 120° with a step size of 0.013° and a total scan time of 2 h. Rietveld refinements of the recorded diffraction patterns was performed using TOPAS 5.0 (Bruker AXS, Karlsruhe, Germany) software.[61] Crystallographic structure and microstructure were refined, while instrumental line broadening was included in a fundamental parameters approach.[62] The mean crystallite size $<L>$ was calculated as the mean volume weighted column height derived from the integral breadth. Crystal structure data were obtained from the Pearson's Crystal database.[63]

Electron paramagnetic resonance (EPR) spectra were recorded using a Bruker Elexsys E580 X-band spectrometer with a Bruker ER 4118X-MD5 resonator. All shown EPR spectra were recorded at 10 K using a closed cycle cryostat (Cryogenic CF VTC).

For the acquisition of the Raman spectra, a Raman microscope LabRAM HR Evolution HORIBA Jobin Yvon A (Longmujeau, France) with a 633 nm He-Ne Laser (Melles Griot, IDEX Optics and Photonics, Albuquerque, USA) and an 1800 lines/mm grating was used.

UV-Vis diffuse reflectance spectra were recorded on a Perkin Elmer Lambda 750 spectrometer (PerkinElmer Inc., Shelton, USA) equipped with a 100 mm integration sphere from 290 to 1500 nm with a 2 nm increment and an integration time of 0.2 s. $BaSO_4$ was used as the white reference.

Thermogravimetric analyses (TGA) were performed on a TG F1 Iris (Netzsch Gerätebau GmbH, Selb, Germany). The samples were first heated from room temperature to 600 °C under nitrogen flow (40 mL min^{-1}) followed by heating to 900 °C under synthetic air (40 mL min^{-1}, N_2/O_2 4:1). The heating rate was set to 20 K min^{-1}.

^{6}Li single-pulse excitation magic angle spinning (SPE MAS) NMR spectra were recorded at 58.91 MHz on a Bruker AV400WB spectrometer (Bruker, Karlsruhe, Germany) at 298 K in standard ZrO_2 rotors with a diameter of 4 mm. A spinning rate of 13 kHz and a relaxation delay of 3 s were applied. Solid LiCl was used as an external reference with a chemical shift of 0 ppm. Spectra were recorded using the TopSpin software.[64] Fitting of the spectra was performed using the DMFit software program package.[65]

The elemental quantification was conducted via inductively coupled plasma mass spectrometry (ICP-MS) with a commercial ICP-MS system (8900 Triple Quad and SPS4 autosampler, Agilent, Santa Clara, USA). Stock solutions of single element ICP-MS standards of Li^+ (Merck Millipore, Darmstadt, Germany), Ti^{4+} (VWR, Radnor, USA) and Sc^{3+} (Merck Millipore, Darmstadt, Germany) were used. The detector dwell time was 100 μs, the repetition was 3 times, and the measured isotopes were ^{7}Li in no-gas mode and ^{47}Ti using He as collision gas as well as ^{45}Sc (all used modes) as internal standard. For the ICP-MS measurements, the washed samples were dissolved in H_2SO_4 (Fisher Chemical, Loughborough, United Kingdom, ≥95%).

Elemental analysis was performed using a Vario Micro Cube CHN analyzer (Elementar, Langenselbold, Germany).

Acknowledgements

We thank Dr. Kristina Brix for the ICP-MS, Dr. Petra Herbeck-Engel for Raman, Dr. Clemens Matt for EPR and Dr. Michael Zimmer for NMR measurements. Instrumentation and technical support for this work were provided by the Service Center NMR at UdS, with financial support from Saarland University and German Science Foundation DFG. Additionally, instrumentation and technical assistance were provided by the Service Center X-ray Diffraction, with financial support from Saarland University

and German Science Foundation (project number INST 256/349-1). Open Access funding enabled and organized by Projekt DEAL.

Conflict of Interest

The authors declare no conflict of interests.

Data Availability Statement

The data that support the findings of this study are available in the supplementary material of this article.

Keywords: black niobia · black titania · hydrides · mechanochemistry · solid-state reactions

[1] X. Chen, L. Liu, F. Huang, *Chem. Soc. Rev.* **2015**, *44*, 1861–1885.
[2] X. Chen, L. Liu, P. Y. Yu, S. S. Mao, *Science* **2011**, *331*, 746–750.
[3] a) H. Cui, G. Zhu, Y. Xie, W. Zhao, C. Yang, T. Lin, H. Gu, F. Huang, *J. Mater. Chem. A* **2015**, *3*, 11830–11837; b) W. Zhao, W. Zhao, G. Zhu, T. Lin, F. Xu, F. Huang, *Dalton Trans.* **2016**, *45*, 3888–3894.
[4] A. Sinhamahapatra, J.-P. Jeon, J. Kang, B. Han, J.-S. Yu, *Sci. Rep.* **2016**, *6*, 27218.
[5] T. Matsukawa, T. Ishigaki, *Dalton Trans.* **2021**, *50*, 7590–7596.
[6] A. Badreldin, M. D. Imam, Y. Wubulikasimu, K. Elsaid, A. E. Abusrafa, P. B. Balbuena, A. Abdel-Wahab, *J. Alloys Compd.* **2021**, *871*, 159615.
[7] H.-S. Kim, J. B. Cook, H. Lin, J. S. Ko, S. H. Tolbert, V. Ozolins, B. Dunn, *Nat. Mater.* **2017**, *16*, 454–462.
[8] a) H. Tan, Z. Zhao, M. Niu, C. Mao, D. Cao, D. Cheng, P. Feng, Z. Sun, *Nanoscale* **2014**, *6*, 10216–10223; b) L. Han, Z. Ma, Z. Luo, G. Liu, J. Ma, X. An, *RSC Adv.* **2016**, *6*, 6643–6650.
[9] Z. Wang, C. Yang, T. Lin, H. Yin, P. Chen, D. Wan, F. Xu, F. Huang, J. Lin, X. Xie, M. Jiang, *Energy Environ. Sci.* **2013**, *6*, 3007–3014.
[10] a) S.-T. Myung, M. Kikuchi, C. S. Yoon, H. Yashiro, S.-J. Kim, Y.-K. Sun, B. Scrosati, *Energy Environ. Sci.* **2013**, *6*, 2609–2614; b) B. Santara, P. K. Giri, K. Imakita, M. Fujii, *Nanoscale* **2013**, *5*, 5476–5488.
[11] a) A. Sinhamahapatra, J.-P. Jeon, J.-S. Yu, *Energy Environ. Sci.* **2015**, *8*, 3539–3544; b) M. Ye, J. Jia, Z. Wu, C. Qian, R. Chen, P. G. O'Brien, W. Sun, Y. Dong, G. A. Ozin, *Adv. Energy Mater.* **2017**, *7*, 1601811.
[12] W. Fang, M. Xing, J. Zhang, *Appl. Catal. B* **2014**, *160–161*, 240–246.
[13] M. Zhang, Q. Pei, W. Chen, L. Liu, T. He, P. Chen, *RSC Adv.* **2017**, *7*, 4306–4311.
[14] G. Ou, Y. Xu, B. Wen, R. Lin, B. Ge, Y. Tang, Y. Liang, C. Yang, K. Huang, D. Zu, R. Yu, W. Chen, J. Li, H. Wu, L.-M. Liu, Y. Li, *Nat. Commun.* **2018**, *9*, 1302.
[15] X. Zhou, N. Liu, J. Schmidt, A. Kahnt, A. Osvet, S. Romeis, E. M. Zolnhofer, V. R. R. Marthala, D. M. Guldi, W. Peukert, M. Hartmann, K. Meyer, P. Schmuki, *Adv. Mater.* **2017**, *29*, 1604747.
[16] R. D. Shannon, *Acta Crystallogr. Sect. A* **1976**, *32*, 751–767.
[17] C. E. Housecroft, A. G. Sharpe, *Inorganic Chemistry*, Pearson Education Limited, **2008**, p. 279.
[18] J. Zhang, P. Zhou, J. Liu, J. Yu, *Phys. Chem. Chem. Phys.* **2014**, *16*, 20382–20386.
[19] R. Ren, Z. Yang, L. L. Shaw, *J. Mater. Sci.* **2000**, *35*, 6015–6026.
[20] A. Le Viet, R. Jose, M. V. Reddy, B. V. R. Chowdari, S. Ramakrishna, *J. Phys. Chem. C* **2010**, *114*, 21795–21800.
[21] K. Su, H. Liu, Z. Gao, P. Fornasiero, F. Wang, *Adv. Sci.* **2021**, *8*, 2003156.
[22] H. Guo, A. Jaworski, Z. Ma, A. Slabon, Z. Bacsik, R. Nedumkandathil, U. Häussermann, *RSC Adv.* **2020**, *10*, 35356–35365.
[23] B. C. Hernden, J. A. Lussier, M. Bieringer, *Inorg. Chem.* **2015**, *54*, 4249–4256.
[24] G. Greenwood, *Phil. Mag.* **1924**, *48*, 654–663.
[25] W. J. H. Borghols, M. Wagemaker, U. Lafont, E. M. Kelder, F. M. Mulder, *Chem. Mater.* **2008**, *20*, 2949–2955.
[26] D. W. Murphy, R. J. Cava, S. M. Zahurak, A. Santoro, *Solid State Ionics* **1983**, *9–10*, 413–417.
[27] M. Vijayakumar, S. Kerisit, C. Wang, Z. Nie, K. M. Rosso, Z. Yang, G. Graff, J. Liu, J. Hu, *J. Phys. Chem. C* **2009**, *113*, 14567–14574.
[28] R. J. Cava, D. W. Murphy, S. M. Zahurak, *J. Electrochem. Soc.* **1983**, *130*, 2345–2351.
[29] C. Valencia-Balvín, S. Pérez-Walton, G. M. Dalpian, J. M. Osorio-Guillén, *Comput. Mater. Sci.* **2014**, *81*, 133–140.
[30] M. Catti, M. R. Ghaani, *Phys. Chem. Chem. Phys.* **2014**, *16*, 1385–1392.
[31] C. Dwivedi, T. Mohammad, V. Kumar, V. Dutta, *Vacuum* **2020**, *182*, 109612.
[32] H. Schäfer, R. Gruehn, F. Schulte, *Angew. Chem. Int. Ed.* **1966**, *5*, 40–52; *Angew. Chem.* **1966**, *78*, 28–41.
[33] a) M. V. Koudriachova, N. M. Harrison, S. W. de Leeuw, *Phys. Rev. B* **2002**, *65*, 235423; b) E. Baudrin, S. Cassaignon, M. Koelsch, J.-P. Jolivet, L. Dupont, J.-M. Tarascon, *Electrochem. Commun.* **2007**, *9*, 337–342.
[34] H. Li, Y. Guo, J. Robertson, *J. Phys. Chem. C* **2015**, *119*, 18160–18166.
[35] a) H.-D. Yang, Y.-Y. Kang, P.-P. Zhu, Q.-W. Chen, L. Yang, J.-P. Zhou, *J. Alloys Compd.* **2021**, *872*, 159759; b) D. R. Zhang, H. L. Liu, R. H. Jin, N. Z. Zhang, Y. X. Liu, Y. S. Kang, *J. Ind. Eng. Chem.* **2007**, *13*, 92–96.
[36] J. Chaudhuri, M. L. Ram, B. K. Sarkar, *J. Mater. Sci.* **1994**, *29*, 3484–3488.
[37] a) X. Chen, L. Liu, Z. Liu, M. A. Marcus, W.-C. Wang, N. A. Oyler, M. E. Grass, B. Mao, P.-A. Glans, P. Y. Yu, J. Guo, S. S. Mao, *Sci. Rep.* **2013**, *3*, 1510; b) Z. Wang, C. Yang, T. Lin, H. Yin, P. Chen, D. Wan, F. Xu, F. Huang, J. Lin, X. Xie, M. Jiang, *Adv. Funct. Mater.* **2013**, *23*, 5444–5450; c) Z. Zheng, B. Huang, J. Lu, Z. Wang, X. Qin, X. Zhang, Y. Dai, M.-H. Whangbo, *Chem. Commun.* **2012**, *48*, 5733–5735.
[38] X. Liu, G. Zhu, X. Wang, X. Yuan, T. Lin, F. Huang, *Adv. Energy Mater.* **2016**, *6*, 1600452.
[39] a) R. Nedumkandathil, A. Jaworski, J. Grins, D. Bernin, M. Karlsson, C. Eklöf-Österberg, A. Neagu, C.-W. Tai, A. J. Pell, U. Häussermann, *ACS Omega* **2018**, *3*, 11426–11438; b) Y. Kobayashi, Z. Li, K. Hirai, C. Tassel, F. Loyer, N. Ichikawa, N. Abe, T. Yamamoto, Y. Shimakawa, K. Yoshimura, M. Takano, O. J. Hernandez, H. Kageyama, *J. Solid State Chem.* **2013**, *207*, 190–193.
[40] B. Oberhausen, G. Kickelbick, *Nanoscale Adv.* **2021**, *3*, 5589–5604.
[41] S. Zhang, G. Liu, W. Qiao, J. Wang, L. Ling, *J. Colloid Interface Sci.* **2020**, *562*, 193–203.
[42] A. Deschanvres, B. Raveau, Z. Sekkal, *Mater. Res. Bull.* **1971**, *6*, 699–704.
[43] B. M. Gatehouse, P. Leverett, *Acta Crystallogr. Sect. C* **1972**, *1*, 83–86.
[44] a) S. Britto, M. Leskes, X. Hua, C.-A. Hébert, H. S. Shin, S. Clarke, O. Borkiewicz, K. W. Chapman, R. Seshadri, J. Cho, C. P. Grey, *J. Am. Chem. Soc.* **2015**, *137*, 8499–8508; b) M. Wagemaker, R. van de Krol, A. P. M. Kentgens, A. A. van Well, F. M. Mulder, *J. Am. Chem. Soc.* **2001**, *123*, 11454–11461; c) K. Hoshina, Y. Harada, H. Inagaki, N. Takami, *J. Electrochem. Soc.* **2014**, *161*, A348-A354; d) M. Vijayakumar, S. Kerisit, K. M. Rosso, S. D. Burton, J. A. Sears, Z. Yang, G. L. Graff, J. Liu, J. Hu, *J. Power Sources* **2011**, *196*, 2211–2220; e) D. Becker, R. Haberkorn, G. Kickelbick, *Inorganics* **2018**, *6*, 117.
[45] C. Pan, Y. J. Lee, B. Ammundsen, C. P. Grey, *Chem. Mater.* **2002**, *14*, 2289–2299.
[46] a) R. Pöttgen, T. Dinges, H. Eckert, P. Sreeraj, H.-D. Wiemhöfer, *Z. Phys. Chem.* **2010**, *224*, 1475–1504; b) T. Dinges, R.-D. Hoffmann, L. van Wüllen, P. Henry, H. Eckert, R. Pöttgen, *J. Solid State Electrochem.* **2011**, *15*, 237–243.
[47] P. F. Chester, *J. Appl. Phys.* **1961**, *32*, 866–868.
[48] Y. Su, J. Lang, L. Li, K. Guan, C. Du, L. Peng, D. Han, X. Wang, *J. Am. Chem. Soc.* **2013**, *135*, 11433–11436.
[49] S. P. S. Porto, P. A. Fleury, T. C. Damen, *Phys. Rev.* **1967**, *154*, 522–526.
[50] A. A. McConnell, J. S. Aderson, C. N. R. Rao, *Spectrochim. Acta Part A* **1976**, *32*, 1067–1076.
[51] V. V. Strelchuk, S. I. Budzulyak, I. M. Budzulyak, R. V. Ilnytsyy, V. O. Kotsyubynskyy, M. Y. Segin, L. S. Yablon, *Semicond. Phys. Quantum Electron. Optoelectron.* **2010**, *13*, 309–313.
[52] S. K. Gautam, F. Singh, I. Sulania, R. G. Singh, P. K. Kulriya, E. Pippel, *J. Appl. Phys.* **2014**, *115*, 143504.
[53] S. Landi Jr., I. R. Segundo, E. Freitas, M. Vasilevskiy, J. Carneiro, C. J. Tavares, *Solid State Commun.* **2022**, *341*, 114573.
[54] a) Y. Jia, M. Zhong, F. Yang, C. Liang, H. Ren, B. Hu, Q. Liu, H. Zhao, Y. Zhang, Y. Zhao, *J. Phys. Chem. C* **2020**, *124*, 15066–15075; b) S. Sathasivam, B. A. D. Williamson, S. A. Althabaiti, A. Y. Obaid, S. N. Basahel, M. Mokhtar, D. O. Scanlon, C. J. Carmalt, I. P. Parkin, *ACS Appl. Mater. Interfaces* **2017**, *9*, 18031–18038; c) I. Erdem, H. H. Kart, *Mater. Sci. Semicond. Process.* **2014**, *28*, 59–65; d) M. Landmann, E. Rauls, W. G. Schmidt, *J. Phys. Condens. Matter.* **2012**, *24*, 195503.
[55] P. O. Oladoye, T. O. Ajiboye, E. O. Omotola, O. J. Oyewola, *Results Eng.* **2022**, *16*, 100678.

[56] A. P. Amrute, J. De Bellis, M. Felderhoff, F. Schüth, *Chem. Eur. J.* **2021**, *27*, 6819–6847.
[57] K. Saitow, T. Wakamiya, *Appl. Phys. Lett.* **2013**, *103*, 031916.
[58] W. Ashraf, A. Khan, S. Bansal, M. Khanuja, *Physica E Low Dimens. Syst. Nanostruct.* **2022**, *140*, 115152.
[59] a) M. Ye, J. Pan, Z. Guo, X. Liu, Y. Chen, *Nanotechnol. Rev.* **2020**, *9*, 558–567; b) J. Zhou, M. Zhang, Y. Zhu, *Phys. Chem. Chem. Phys.* **2015**, *17*, 3647–3652.
[60] M. K. Kim, W. H. Sim, M. Choi, H. Lim, Y. Kwon, H. M. Jeong, *Catal. Today* **2021**, *359*, 23–27.
[61] Bruker AXS, *Topas 5*, Karlsruhe, Germany, **2014**.
[62] R. W. Cheary, A. A. Coelho, J. P. Cline, *J. Res. Natl. Inst. Stand. Technol.* **2004**, *109*, 1–25.
[63] P. Villars, K. Cenzual, Pearson's Crystal Data: Crystal Structure Database for Inorganic Compounds (on DVD), Release 2022/23, ASM International®, Materials Park, Ohio, USA
[64] Bruker Corp., *Topspin 2.1*, Karlsruhe, Germany, **2008**.
[65] D. Massiot, F. Fayon, M. Capron, I. King, S. Le Calvé, B. Alonso, J.-O. Durand, B. Bujoli, Z. Gan, G. Hoatson, *Magn. Reson. Chem.* **2002**, *40*, 70–76.

Manuscript received: January 23, 2023
Accepted manuscript online: February 10, 2023
Version of record online: April 5, 2023